Enhancing combustion performance of nano-Al/PVDF composites with β-PVDF

Sidi Huang [a,1], Sungwook Hong [b,c,1], Yingchun Su [e], Yue Jiang [a], Shogo Fukushima [d], Thomas Mark Gill [a], Nil Ezgi Dincer Yilmaz [a], Subodh Tiwari [b], Ken-ichi Nomura [b], Rajiv K. Kalia [b], Aiichiro Nakano [b], Fuyuki Shimojo [d], Priya Vashishta [b], Menglin Chen [e], Xiaolin Zheng [a,*]

[a] Department of Mechanical Engineering, Stanford University, , Building 520, Room 223, CA 94305, USA
[b] Collaboratory for Advanced Computing and Simulations, Department of Physics and Astronomy, Department of Computer Science, Department of Chemical Engineering and Materials Science, and Department of Biological Sciences, University of Southern California, Los Angeles, CA 90089-0242, USA
[c] Department of Physics and Engineering, California State University, Bakersfield, Bakersfield, CA 93311, USA
[d] Department of Physics, Kumamoto University, Kumamoto 860-8555, Japan
[e] Department of Engineering, Interdisciplinary Nanoscience Center, Aarhus University, Aarhus, DK-8000, Denmark

ARTICLE INFO

ABSTRACT

Solid energetic nanocomposites, consisting of reactive metal particles and oxidizers, find broad applications ranging from pyrotechnics to solid rocket propellants and solid ramjet fuels. In particular, nano-aluminum (n-Al) and polyvinylidene fluoride (PVDF) are attractive fuel and oxidizer materials, due to the high energy density of n-Al, and the high oxidizing potential and excellent mechanical properties of PVDF. PVDF is a semi-crystalline polymer and has three common crystalline phases, alpha (α), gamma (γ), and beta (β) phases. Many research works have focused on the chemical reactions between Al and PVDF, yet the effect of PVDF crystallinity on the Al/PVDF reaction is unknown. Here, we experimentally and computationally demonstrate that increasing the mass fraction of β-phase PVDF from 2.5 to 25% in Al/PVDF composites substantially improves peak pressure by 90% (from ~34 to ~64 psi) and pressure rise rates by 300% (from 2.5 psi/ms to 10 psi/ms). This stems from the alignment of F atoms along one side of the β-PVDF polymer chain, making it structurally conducive to reacting with Al particles to form strong Al-F interactions. This strong interaction leads to higher binding energy between, and hence higher reactivity in, β-PVDF and Al. Our research provides a new method for enhancing the reactive performance of Al/PVDF composites by increasing the content of β-PVDF.

1. Introduction

Solid energetic composites consisting of fuels and oxidizers readily generate heat, gases, and light, and hence are widely used in pyrotechnics, initiators, solid-propellant rockets, and solid ramjet fuels [1–3]. For such composites, an interesting metal fuel is nano-aluminum (nAl) due to its earth abundance, high specific energy density (31 kJ/g for Al oxidization), and low ignition threshold [2]. Typical oxidizers include metal oxides [4–6], perchlorate salts [7], and fluorine-based polymer [8,9]. Among these, fluorine (F)-based polymers are particularly attractive as oxidizers because F can react both with Al and its native oxide Al_2O_3 to form AlF_3, which has a lower boiling temperature than Al_2O_3 and facilitates the exposure of fresh Al for the further reaction [10–12]. Also, the heat of reaction of Al fluorination by F_2 is much higher than that of Al oxidation by O_2 (55.7 kJ/g vs. 31 kJ/g) [11]. Another benefit of fluorine-based polymers is that they can serve as binders to provide energetic composites with mechanical integrity [13]. Many fluorine-based polymers have been tested for Al combustion, including polyvinylidene fluoride (PVDF) [4], polytetrafluoroethylene (PTFE) [8,14], tetrafluoroethylene-hexafluoropropylene-vinylidene fluoride (THV) [13], and hexafluoropropylene and vinylidene fluoride (Viton) [13]. Among these polymers, PTFE has the highest fluorine content (~76 wt%), but it is largely insoluble in common solvents which limits its use as a binder [13]. In comparison, PVDF with a fluorine

content of 59.4 wt% is of great interest due to its great mechanical strength, interesting electrical properties (*e.g.*, ferro-, piezo-, and pyro-electricity), good thermal and chemical stability, and easy dissolution in many solvents [15–18]. Furthermore, Al/PVDF was shown to have better tensile elasticity and burn rates than other Al/fluoropolymers, such as Al/THV and Al/Viton composites [13].

Despite the abovementioned possible advantages of Al/PVDF energetic composite, the energy release rate (*e.g.*, burning rate) of is slower than that of nAl/PTFE composite [16,19]. The burning rate of 30 wt% is 15 cm/s [16], which is 10 times lower than the burning rate of 30 wt% nAl/PTFE (150 cm/s) [19]. Several methods have been reported to increase the energy release rates of nAl/PVDF [20–22]. One method adds mesoporous silica into the composite, for which the mesoporous silica reduces the decomposition temperature of PVDF, increasing the burning rate to 35 cm/s [20]. Another method improves the energy release rate of nAl/PVDF by achieving uniform dispersion of nAl in PVDF through a modified microemulsion method [21]. The third method modifies the micro-architecture of nAl/PVDF composites by producing electro-spun nAl/PVDF fibers, which demonstrates the highest burning rate (~60 cm/s) and lowest ignition temperature (~780°C) among 3D printed and electro-sprayed nAl/PVDF composites [22].

These methods have significantly improved the combustion performance of nAl/PVDF composites, making nAl/PVDF even more attractive for energetic applications. However, the effect of the crystalline phase of PVDF on the combustion performance of n-Al/PVDF has not been reported. PVDF is a semi-crystalline thermoplastic polymer with five possible polymorphs: α, β, γ, δ, and ε phases [23,24]. Among them, α-, β-, and γ-PVDF are commonly formed and used [24,25]. β-PVDF is of particular interest due to its pyro-, piezo-, and ferroelectricity from its spontaneous polarization [25,26]. For energetic materials, the piezoelectric effect was not a commonly studied property. Several studies have demonstrated that the piezoelectric effect improves the ignition performance of nAl/PVDF, nAl/THV, and nAl/Viton composites presumably by generating charges that convert to localized "hot spots" [27–29]. In addition, DFT calculations revealed that β-PVDF is the least chemically stable phase among all common PVDF crystalline phases [30,31]. Therefore, it is of great interest to investigate the effect of β-PVDF content on the combustion performance of nAl/PVDF due to the possibility of enhancing the inherent reactivity of the composite through phase composition control.

Here, we report the first experimental and reactive molecular dynamics (RMD) study on the effect of β-phase fraction in PVDF on the combustion performance of nAl/PVDF composite. We achieved different fractions of β-phase PVDF in the nAl/PVDF composites by using three fabrication methods, including rod rolling to make nAl/PVDF films, porous template casting to make nAl/PVDF sponges, and electro-spinning to make nAl/PVDF fibers. The mass fraction of β-phase PVDF (D (β)) in all samples is quantified by Fourier-transform infrared spectroscopy (FTIR) and differential scanning calorimetry (DSC). The electron-spun nAl/PVDF fibers have the highest mass fraction of β-phase PVDF. The combustion performance of all samples is evaluated in terms of peak pressure, pressure rise rate, and heat of reaction as determined in a constant-volume reactor. We found that the combustion performance of all samples increases with increasing β-PVDF mass fraction. These experimental results were supported by our RMD simulations, which reveal that among the three different phases of PVDF studied, the reactivity of the nAl/β-PVDF system is higher than that of other systems because β-PVDF has stronger binding energy to the oxide layer of Al, compared with α-PVDF or γ-PVDF.

2. Experimental specifications

2.1. Synthesis of nAl/PVDF composites with different contents of β-PVDF

We prepared three types of nAl/PVDF composites using different fabrication methods (Fig. 1), including rod rolling to make nAl/PVDF films, porous template casting to make nAl/PVDF sponges, and electro-spinning to make nAl/PVDF fibers. For all nAl/PVDF composites, we used Al nanoparticles (average diameter: 70 nm) from U.S. Research Nanomaterials. The active content of 70 nm Al nanoparticles is 72.5 % as previously determined from thermogravimetric analysis (TGA) [21]. We used PVDF (Avg. molecular weight =180,000) from Sigma Aldrich Inc. Both Al nanoparticles and PVDF powders were used as received. All the nAl/PVDF composites are set to be stoichiometric (Φ=1, 28 wt% Al and 72 wt% PVDF) based on the active content of Al particles.

All samples were prepared by two steps: (1) mixing nAl and PVDF to form a precursor solution and (2) casting the precursor solutions into different morphologies (Fig. 1(a)–(c)). For both the nAl/PVDF film (Fig. 1(a)) and sponge (Fig. 1(b)), the precursor solution was prepared by the modified micro-emulsion method (μE) due to its ability to uniformly disperse Al particles in PVDF[21]. The principle of the modified micro-emulsion method is that a volatile hexane micron-sized droplet encapsulates a few oleic acid functionalized Al nanoparticles in a PVDF and dimethyl-formamide (DMF) polymer solution. Upon the evaporation of hexane solvent, the high viscosity of PVDF/DMF polymer solution prevents Al nanoparticles from merging, leading to finely dispersed Al nanoparticles. The nAl/PVDF film was made by drop-casting nAl/PVDF/DMF precursor solution onto a borosilicate glass, followed by rolling with a Mayer rod. The Al/PVDF film was obtained after the DMF solvent evaporated at 55 °C (Fig. 1(d)). The nAl/PVDF sponge was obtained by drop-casting nAl/PVDF/DMF precursor solution in a porous sugar cube template. After dissolving the sugar cube template in water, the nAl/PVDF sponge remained (Fig. 1(e)). For the nAl/PVDF fibers (Fig. 1(c)), the Al/PVDF precursor solution was prepared by the mechanical mixing (MM) method, not the micro-emulsion method, as the micro-emulsion prepared precursor does not have suitable viscosity for the electro-spinning process. The nAl/PVDF (Fig. 1(f)) fiber was attained by electro-spinning nAl/PVDF/DMF precursor solution onto an aluminum foil collector at different voltages (e.g., 13kV, 15kV, 17kV and 19kV).

2.1.1. Synthesis of nAl/PVDF film using rod rolling method

Our previous work has reported a method to prepare stoichiometric nAl/PVDF film precursor solutions [21]. Typically, 195 mg of Al nanoparticles (average diameter: 70 nm) was dispersed in 130 mL of hexane and sonicated for 25 min to break up Al particle aggregates. 1 mL of oleic acid was subsequently added to the Al solution and stirred for 1 h to functionalize the surface of Al particles with oleic acid (OA). We previously used FTIR and XPS to confirm the presence of OA on the nAl particle surface and determined that the mass change of Al particles before and after oleic acid is negligibly small [21]. Then, oleic acid functionalized nAl particles (OA-Al) was further sonicated in 3 mL of hexane co-solvent for 1 h. In the meantime, 500 mg of PVDF pellets (Avg. molecular weight = 180,000) was dissolved in 3 mL of DMF solvent. The PVDF/DMF solution was vigorously stirred by a magnetic bar at 60 °C for 3 hours until PVDF pellets were fully dissolved in the DMF solvent. The PVDF/DMF solution was placed in a desiccator under a dynamic vacuum for 20 min to remove gas bubbles. The sonicated OA-Al in hexane co-solvent was immediately mixed with PVDF/DMF solution, followed by vigorous stirring at 65 °C for 1 h. During the stirring, the hexane co-solvent would evaporate, leaving dispersed Al particles in the PVDF/DMF solution. The re-
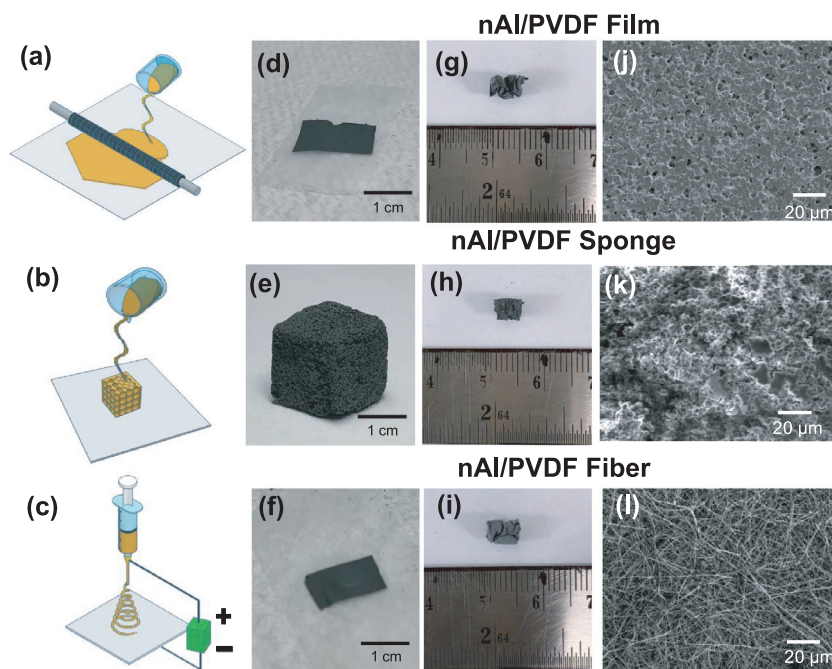
Fig. 1. Schematic of the (a) rod rolling, (b) porous template casting, and (c) electro-spinning deposition method to fabricate nAl/PVDF composites. Photographs of the as-synthesized (d) nAl/PVDF film, (e) nAl/PVDF sponge, and (f) nAl/PVDF fiber electro-spun at 17 kV. Photographs of the compressed pellets of (g) nAl/PVDF film, (h) nAl/PVDF sponge, and (i) nAl/PVDF fiber electro-spun at 17 kV. Each pellet weighs ~20 mg and has a diameter of ~ 3 mm and a height of ~5 mm. The pellet forms were used for the specific surface area and all combustion experiments. SEM images showing the surface morphologies of the pellets of (j) nAl/PVDF film, (k) nAl/PVDF sponge, and (l) nAl/PVDF fiber electro-spun at 17kV.

sulting nAl/PVDF/DMF solution was gently dispersed on a cleaned borosilicate glass sheet (McMaster-Carr Inc.). A Mayer rod (Type 90) was rolled over the nAl/PVDF/DMF solution to form a uniform nAl/PVDF/DMF film. The resulting nAl/PVDF/DMF film was placed on a hot plate at 55 °C until the DMF solvent has completely evaporated. The nAl/PVDF film was cooled to room temperature in air and peeled off the borosilicate glass using a razor blade.

2.1.2. Synthesis of nAl/PVDF sponge using the porous template casting method

The stoichiometric nAl/PVDF sponge precursor solution was prepared the same way as the nAl/PVDF film precursor solution. The nAl/PVDF/DMF precursor solution was drop-cast onto a sugar cube template to form the nAl/PVDF/DMF sponge composite. The sponge composite was dried under vacuum overnight and further immersed in water at 55 °C for 5 h to dissolve the sugar template. The nAl/PVDF sponge was finally dried at room temperature in air.

2.1.3. Synthesis of nAl/PVDF fiber using the electrospinning method

For a typical stoichiometric 70 nm nAl/PVDF fibers, 0.875 g of Al nanoparticles was sonicated in 5 mL of DMF solution for 1 h. After the sonication, 2.25 g of PVDF pellets were dissolved in the mixture solution and heated in a water bath at 60 °C until all PVDF pellets were dissolved in DMF solution. Then, the nAl/PVDF/DMF precursor solution was placed in a 3 mL syringe fitted with a metallic needle of 0.9 mm inner diameter. The distance between the tip of the needle and the grounded aluminum foil wrapped collector was controlled to be 15 cm. The electrospinning process was carried out at applied voltages of 13 kV, 15 kV, 17 kV, and 19 kV with a feeding rate of 0.5 mL/h at 55 °C for 5 h to obtain the Al/PVDF fibers. The nAl/PVDF nanofibers were finally dried under vacuum overnight.

2.2. Thermal analysis of nAl/PVDF specimens

The isothermal heat flow and weight changes of different nAl/PVDF composites were investigated by simultaneous thermogravimetric analysis and differential scanning calorimetry (TGA/DSC, Labsys Evo). For a typical test, approximately 3 mg of the sample was placed into an alumina crucible. The TGA/DSC chamber was first flushed with argon (100 sccm) for 30 min to remove residual oxygen and then the sample was heated in Ar (40 sccm) from 100 to 800 °C (373–1073 K) at a heating rate of 5 °C/min (5 K/min).

2.3. Pressure evolution measurements in a constant-volume vessel

The pressure rise of various nAl/PVDF composites under Ar condition was quantified in a constant-volume vessel (volume: 16 cm^3), in which a similar experimental setup has been discussed previously [32–34]. For a typical test, approximately 20 mg of the sample was loaded in a customized tube with an inner diameter of 3 mm and then compressed into a pellet of 3 mm diameter and 5 mm height. The pellet was placed in an alumina crucible embedded with a Nickel-Chrome fuse wire. Then, the constant-volume vessel was vacuumed and flushed with Ar three times to minimize any residual oxygen in the vessel. The sample was ignited by applying a constant current of 3.15 A from a power supply (2420 3A Souremeter, Keithley, Inc.) to the hotwire. The dynamic vessel pressure was recorded by a pressure transducer (603B1, Kistler Inc.).

2.4. The heat of reaction measurements

The heat of reaction was measured using a bomb calorimeter (6725 Semi-micro Calorimeter, Parr Instrument). For a typical test, 40 mg of the sample was placed in a stainless-steel pan with a Nickel-Chrome fuse wire and encapsulated in a stainless-steel cell.

Before each test, the bomb calorimeter was vacuumed and then flushed with Ar three times to minimize any residual oxygen so that only the heat of reaction between nAl and PVDF was measured. The bomb calorimeter measurement provides the specific heat release of the sample. The basic principle of using the bomb calorimeter to determine the heat of reaction of the sample was discussed in our previous work [21].

2.5. RMD simulations

RMD simulations were performed using the ReaxFF reactive force field [35,36]. Initial force field parameters for Al/C/H/O/F interactions were taken from Hong and van Duin [37]. Rahnamoun and van Duin [38], and Kim et al.[39], and they were merged into a single force field. We then further developed this force field to describe nAl/PVDF interactions. Details about our force field development were discussed in the Supporting Information. We used an orthogonal simulation cell of 43.50Å × 50. 49Å × 47.00Å that contains the Al_2O_3 slab model (1620 atoms) in the middle of the simulation domain while 60 α-PVDF molecules (2100 atoms), 60 β-PVDF molecules (2100 atoms) or 60 γ-PVDF molecules (2100 atoms) are randomly distributed in the remaining vacuum layers. The total number of atoms is 3720 for the simulations. The simulation domain was completely periodic in the x-, y-, and z-directions. The NVT ensemble (i.e., a constant number of atoms, a constant-volume, and a constant temperature) with the Nose-Hoover thermostat [40,41] was applied to the entire system; We used a relatively small time step of 0.25 fs to reasonably capture the reaction processes during RMD simulations with a temperature damping constant of 25.0 fs.

3. Results/discussion

3.1. Material characterizations of different Al/PVDF composites

The as-synthesized nAl/PVDF film, sponge, and fiber have distinct morphologies and porosities (Fig. 1(d)–(f)). To minimize these differences, we further compressed the as-synthesized samples into pellets (20 mg, ~3 mm in diameter and ~5 mm in height) (Fig. 1(g)–(i)) to achieve a similar porosity of around 70%. We acknowledge that some practical applications desire samples of lower porosity, which can be achieved by much stronger compression tools that are difficult to access for laboratory studies. Unless noted, all the nAl/PVDF samples referred to hereafter are compressed pellets. The microscopic morphology differences of those compressed nAl/PVDF pellets were reviewed by scanning electron microscopy (SEM) images. The nAl/PVDF film (Fig. 1(j)) has a smooth surface with some porous features. The nAl/PVDF sponge (Fig. 1(k)) has a rough surface and is highly porous. The nAl/PVDF fiber composite (Fig. 1(l)) consists of fibers with diameters in the sub-micron range. The specific surface areas of compressed nAl/PVDF pellets (Fig. 1(g)–(i)) were determined by the Brunauer-Emmett-Teller (BET) theory with N_2 sorption (Autosorb, iQ2, Quantachrome). The specific surface areas of compressed nAl/PVDF film, sponge and fibers are 7.5 m^2/g, 22.3 m^2/g, and 5.0–7.5 m^2/g, respectively (Fig. 2(a)). The specific surface area of the sponge is about three times those of the film and fibers.

The crystallinity and phase of PVDF in the compressed nAl/PVDF pellets were analyzed by X-ray diffraction (XRD, X'Pert 2, PANalytical) and Fourier transform infrared spectroscopy (FTIR-ATR, Nicolet iS50, Thermo-scientific). The XRD spectra in Fig. 2(b) show that all nAl/PVDF composites exhibit diffraction peaks for crystalline phase nAl and PVDF. The diffraction peak around 18.5° corresponds to monoclinic α-PVDF [25,42], which is observed only for nAl/PVDF fibers. The diffraction peaks around ~ 20–21° can be attributed to either α-, β-, or γ-PVDF[42], which are present for

all samples. The presence of α-, β-, and γ-PVDF in all nAl/PVDF composites is also revealed by the FTIR spectra (Fig. 2(c)), which show sharp peaks around 881, 1071, 1176, and 1401 cm^{-1}, corresponding to α-, β-, and γ-PVDF [25]. The FTIR spectra were used to further quantify the phase percentages of PVDF based on the method proposed by Cai et al. [25]. The method first calculates the total mass fraction of $(\beta+\gamma)$-phase PVDF (Eq. (1)) followed by the fraction of individual β-phase and γ- phase (Eq. (2b)) PVDF [25].

The total mass fraction of $(\beta+\gamma)$/ $(\alpha+\beta+\gamma)$ for PVDF (F_{EA}) is calculated using Eq. (1) below:

$$F_{EA} = \frac{I_{EA}}{\left(\frac{K_{EA}}{K}\right)I + I_{EA}} \times 100\% \qquad (1)$$

, where I_{EA} and I_a are the absorbances at 840 and 763 cm^{-1} in the FTIR spectra, respectively. K_{EA} and K_a are the absorption coefficients at 840 and 763 cm^{-1}, and the values of K_{EA} and K_a are 7.7 × 10^4 and 6.1 × 10^4 cm^2 mol^{-1}, from the literature [25]. The individual fraction of β- and γ-phase PVDF are then calculated using Eqs. (2a) and (2b) [25]:

$$F(\beta) = F_{EA} \times \frac{\Delta H_\beta}{\Delta H_\beta + \Delta H_\beta} \times 100\% \qquad (2a)$$

$$F(\gamma) = F_{EA} \times \frac{\Delta H_\gamma}{\Delta H_\gamma + \Delta H_\gamma} \times 100\% \qquad (2b)$$

$$F(\alpha) = 1 - F(\beta) - F(\gamma) \qquad (3)$$

, where ΔH_β is the height difference (absorbance differences) between the peak around 1275 cm^{-1} and the nearest valley around 1260 cm^{-1}, and ΔH_γ is the height difference between the peak around 1234 cm^{-1} and the nearest valley around 1225 cm^{-1}. The calculated mass fractions of α-, β-, and γ-phase in the crystalline $(\alpha+\beta+\gamma)$ PVDF are plotted in Fig. 2(d). It should be noted that the Al/PVDF composites also contain amorphous PVDF [18,25], so we need to further calculate the total crystalline phase fraction of PVDF to determine the fraction of β-PVDF in the PVDF. This is determined by simultaneous thermogravimetric analysis and differential scanning calorimetry (TGA/DSC, Labsys Evo). Figure 3(a) shows the DSC traces of different nAl/PVDF composites under Ar with a heating rate of 5 °C/min. All composites exhibit a small endothermic peak around 170 °C (443 K), corresponding to the melting temperature of PVDF [43]. The integrated area of this peak gives the measured enthalpy of melting (ΔH_m). The ratio between ΔH_m and the theoretical melt enthalpy for 100% crystalline PVDF (ΔH_c, 104.8 J/g) [44] gives the crystalline mass fraction, W_c, using Eq. (4) [18]. The mass fractions of α, β, and γ-PVDF in the nAl/PVDF mixture, D(α, β, γ), are then calculated by using Eq. (5).

$$W_C = \frac{\Delta H_m}{\Delta H_c} \qquad (4)$$

$$D(\alpha) = W_c \times F(\alpha), \quad D(\beta) = W_c \times F(\gamma), \qquad D(\gamma) = W_c \times F(\gamma) \qquad (5)$$

, where $F(\alpha$, β, and $\gamma)$ is the mass fraction of α, β, and γ-PVDF in the crystalline phase PVDF from the FTIR spectra (Fig. 2(d)). The calculated W_c, D (α), D (γ), and D (β) are plotted in Fig. 3(b). The crystalline phase of PVDF in all samples is about 28–40 wt%. The nAl/PVDF fiber samples have a higher β-PVDF fraction than films and sponges. The reason is that PVDF is polarized by the large electric field during the electrospinning process, which favors the formation of β-PVDF [24]. Higher electro-spun voltage leads to stronger polarizing and thereby a higher fraction of β-PVDF. When the electro-spun voltage reaches 19 kV, Al nanoparticles are agglomerated in PVDF (Fig. S1), reducing the formation of β-PVDF
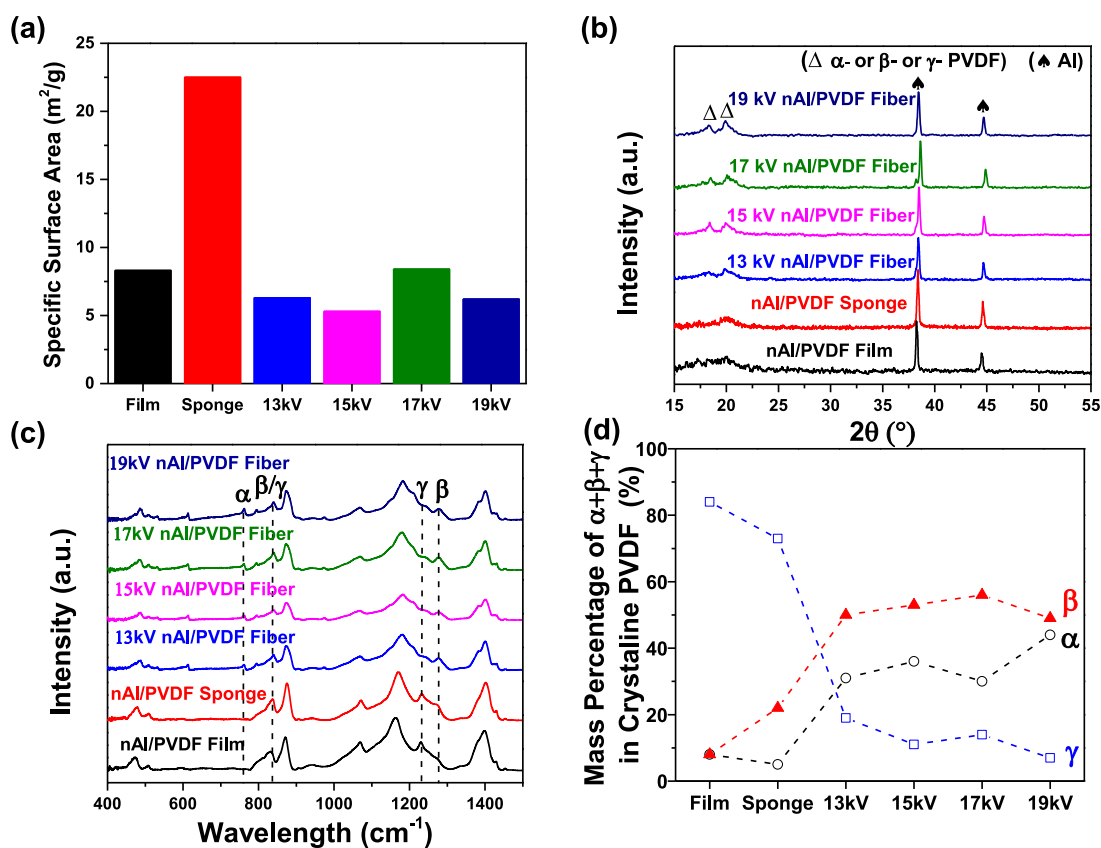
Fig. 2. (a) BET surface areas, (b) XRD spectra, (c) FTIR spectra, and (d) summary of the individual mass fraction of α, β, γ-phase in the crystalline portion of PVDF. The notation of film refers to nAl/PVDF film, sponge refers to nAl/PVDF sponge, and 13,15,17, and 19 kV refer to nAl/PVDF fiber electro-spun at 13kV, 15kV, 17kV and 19kV, respectively. The nAl/PVDF sponge has the highest measured BET surface area, and the nAl/PVDF film and fiber have similar BET surface areas. XRD spectra show strong peaks of Al and α-, β-, γ-PVDF. FTIR spectra reveal that nAl/PVDF fiber has the highest mass fraction of β-PVDF in the crystalline mixture.

in crystalline PVDF [45]. Finally, the nAl/PVDF sponge has a higher fraction of β-PVDF than that of the film because the porosity of the sugar template induces capillary forces on the PVDF during the drying process. The capillary forces stretch the polymer chains of PVDF, promoting the formation of β-PVDF [24,46,47]. The Al/PVDF film has the lowest β-PVDF yet relatively high γ-PVDF content because the DMF solvent tends to re-crystallize PVDF in the γ-phase [44].

The DSC traces in Fig. 3(a), together with the TGA results (Fig. 3(c)), also reveal reaction pathways of different nAl/PVDF composites. For the DSC traces, the first small exothermic peaks around 300–325 °C (573–598 K) correspond to the pre-ignition reaction between the condensed-phase PVDF and the Al_2O_3 shell of the Al particles, as reported by others [16–18]. At the same temperature range, the sample mass starts to decrease (Fig. 3(c)). The larger exothermic peaks around 375–385 °C (648–658 K) and 450–490 °C (723–763 K) correspond to the chemical reaction between decomposed PVDF and the core of Al particles. The endothermic peak around 660 °C (933 K) is attributed to the melting peaks of unreacted Al particles. Finally, a key parameter that describes the degree of reaction between Al and PVDF is the percent weight change of the sample. If PVDF does not react with Al, it will decompose and form gaseous products (e.g., HF), which escape and lead to mass loss [21]. Hence, a higher remaining mass indicates a more complete reaction because Al and PVDF react to form solid AlF_3 (Fig. S2). Here, all nAl/PVDF composites have similar mass remaining (~65–70 wt%) at 800 °C (1073 K), showing little dependence on the crystalline composition of PVDF. This is reasonable as PVDF loses crystallinity after it melts under slow heating conditions, like the conditions present in the DSC/TGA.

3.2. Effect of PVDF crystalline phase on pressure-rise comparison in a constant-volume vessel

Since the above slow heating condition in the DSC/ TGA allows PVDF to lose its crystallinity before reacting with Al, we next studied nAl/PVDF under fast heating conditions to explore the potential beneficial roles of β-PVDF. The pressure rise of various nAl/PVDF composites under Ar condition was quantified in a constant-volume vessel (volume: 16 cm^3), in a previously discussed experimental setup [32–34]. In a typical experiment, one compressed nAl/PVDF pellet (Fig. 1(g)–(i)) was placed in an alumina crucible inside a constant-volume vessel filled with Ar at atmospheric pressure. The compressed nAl/PVDF pellet was ignited by a NiCr hot-wire, and a pressure transducer recorded the dynamic pressure trace from combustion. Three tests were taken for each type of nAl/PVDF composite to determine the average and error bars.

Figure 4(a) shows representative pressure-time traces of the combustion of each of the as-synthesized nAl/PVDF composites measured in the constant-volume vessel setup. We define time zero as the time that pressure starts to rise, corresponding to ignition. After the ignition, pressure sharply rises due to the reaction and then gradually decreases due to the slowing of the reaction, consumption of the products, and nonadiabaticity. These pressure-time traces were further used to determine two parameters: the peak pressure and the pressure rise rate. The peak pressure is the maximum pressure recorded and is associated with the total heat release (i.e., thermal expansion at a constant volume) during the combustion. The pressure rise-rate is the largest slope of the pressure versus time, which is a good indicator of energy release rate
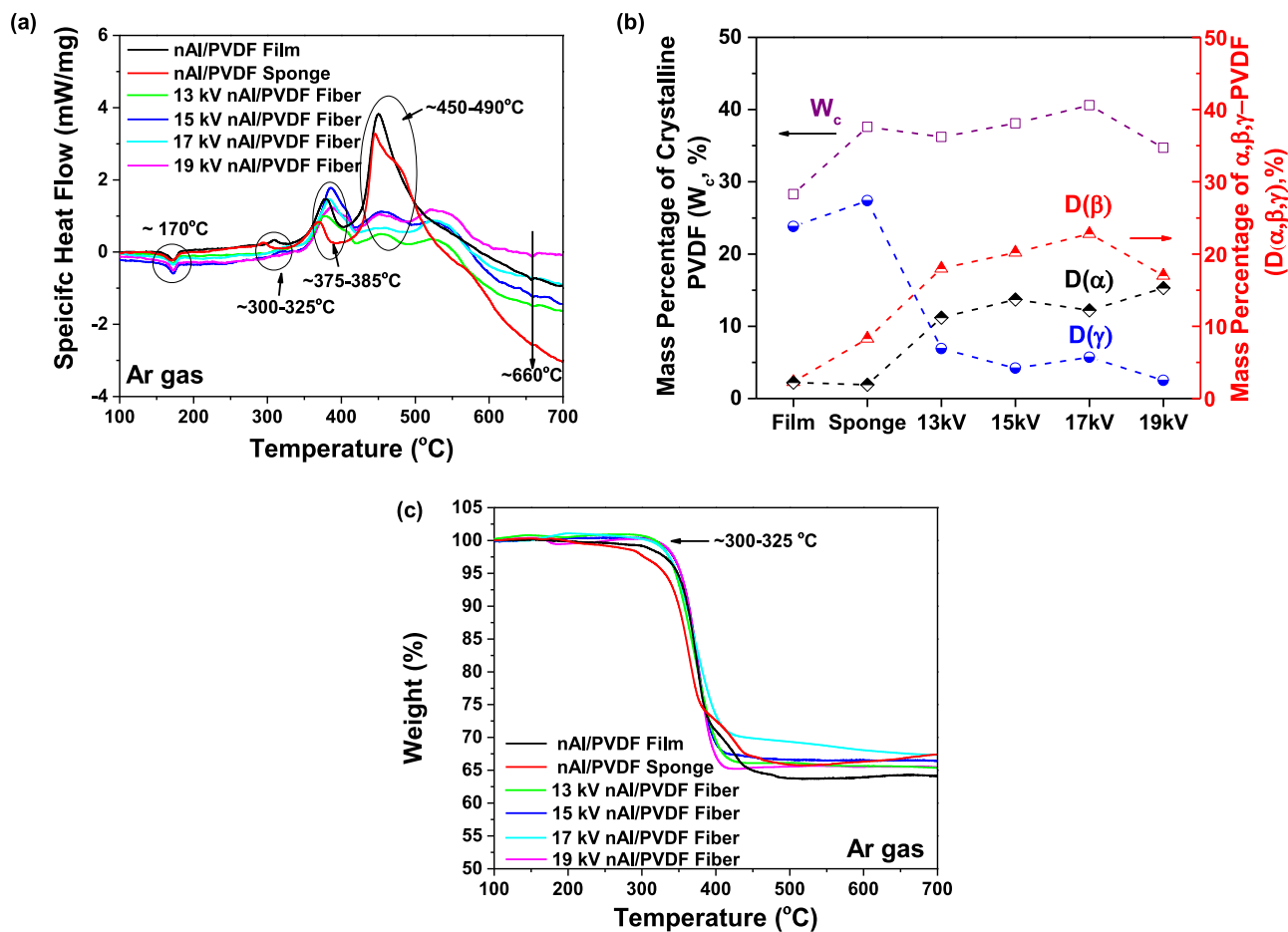
Fig. 3. (a) DSC traces of different nAl/PVDF composites($\Phi=1$). (b) Mass fractions of the total crystalline phase PVDF (W_c), and α,β,γ-phase in PVDF (containing both crystalline and amorphous phase) for different nAl/PVDF mixtures. The 17 kV nAl/PVDF fiber shows the highest W_c and mass fraction of β-PVDF. (c) TGA traces of different nAl/PVDF composites ($\Phi=1$). TGA shows no difference among different nAl/PVDF composites because PVDF loses its crystallinity during melting before reacting with Al.

[48]. Since our compressed nAl/PVDF pellets (Fig. 1(g)–(i)) have a different specific surface area (Fig. 2(a)) and mass fraction of β-PVDF (Fig. 3(b)), we plot the peak pressure and pressure rise rate as a function of specific surface area (Fig. 4(b)) and mass fraction of β-PVDF (Fig. 4(c)) to determine the dominant factor in controlling the combustion pressure characteristics. Clearly, both peak pressure and pressure rise rate show no apparent correlation with the specific surface area, but they increase with increasing mass fraction of β-PVDF (D(β)), not with D(α) or D (γ) (Fig. S3). These results indicate that β-PVDF is beneficial for promoting the reaction between nAl and PVDF.

3.3. Effect of PVDF crystalline phase on the heat of reaction of nAl/PVDF

The constant-volume vessel experiments above show that a higher mass fraction of β-PVDF leads to larger peak pressure and pressure rise rate of compressed nAl/PVDF pellets. We further examine the effect of mass fraction of β-PVDF on the heat of reaction (ΔH) of compressed nAl/PVDF pellets measured in a bomb calorimeter. In a typical test, 40 mg of compressed Al/PVDF composites (Fig. 1(g)–(i)) were placed in a stainless pan and ignited by a NiCr hot-wire in a sealed container filled with Ar to atmospheric pressure. The specific heat of reaction of the sample is normalized by the weight of composite (ΔH, with the unit of J/mg of composite), and Fig. 5 plots the specific heat of reaction of nAl/PVDF composites as a function of the fraction of D(β). Again, a similar trend to Fig. 4(c) is observed, in which the heat of reaction and

combustion efficiency of compressed nAl/PVDF pellets increases as D(β) increases but shows no correlation with D(α) or D(γ) (Figure S4). This result further emphasizes the importance of β-PVDF to enhance the combustion performance of nAl/PVDF composites.

3.4. Chemical reactions of Al_2O_3 and α-, β-, and γ-PVDF by RMD simulations

To gain a molecular-level understanding of the effect of the crystalline phase of PVDF on the combustion performance of nAl/PVDF composites, we constructed three different computational models: 1. Al_2O_3/α-PVDF (Fig. 6(a) and (b)); 2. Al_2O_3/β-PVDF (Fig. 6(c) and (d)); 3. Al_2O_3/γ-PVDF (Fig. 6(e) and (f)). For RMD simulations, we considered the Al_2O_3 slab model instead of the Al slab model because 1) the Al surface is generally covered by Al_2O_3 at room temperature [49,50], and 2) the first step for the chemical reaction between Al and PVDF is the pre-ignition reaction between the Al_2O_3 surface and PVDF [17]. We then ramped the system temperature from 100 K to 1500 K in 350 ps. (i.e., the rate of temperature ramping is 4 K/ps) Fig. 7(a)–(c) shows RMD snapshots of the Al_2O_3/α-PVDF, the Al_2O_3/β-PVDF, and the Al_2O_3/γ-PVDF systems, respectively, at three temperatures (500 K, 1000 K, and 1500 K). Based on our RMD trajectories, β-PVDF molecules are more likely to decompose and react with the Al_2O_3 surface than are α-PVDF or γ-PVDF molecules, thus leading to an increased amount of F-, H-, and C-atom transfer from the PVDF molecules to the Al_2O_3 surface. This prediction is further confirmed by our bond population analysis (Fig. 8). During the RMD simulations of
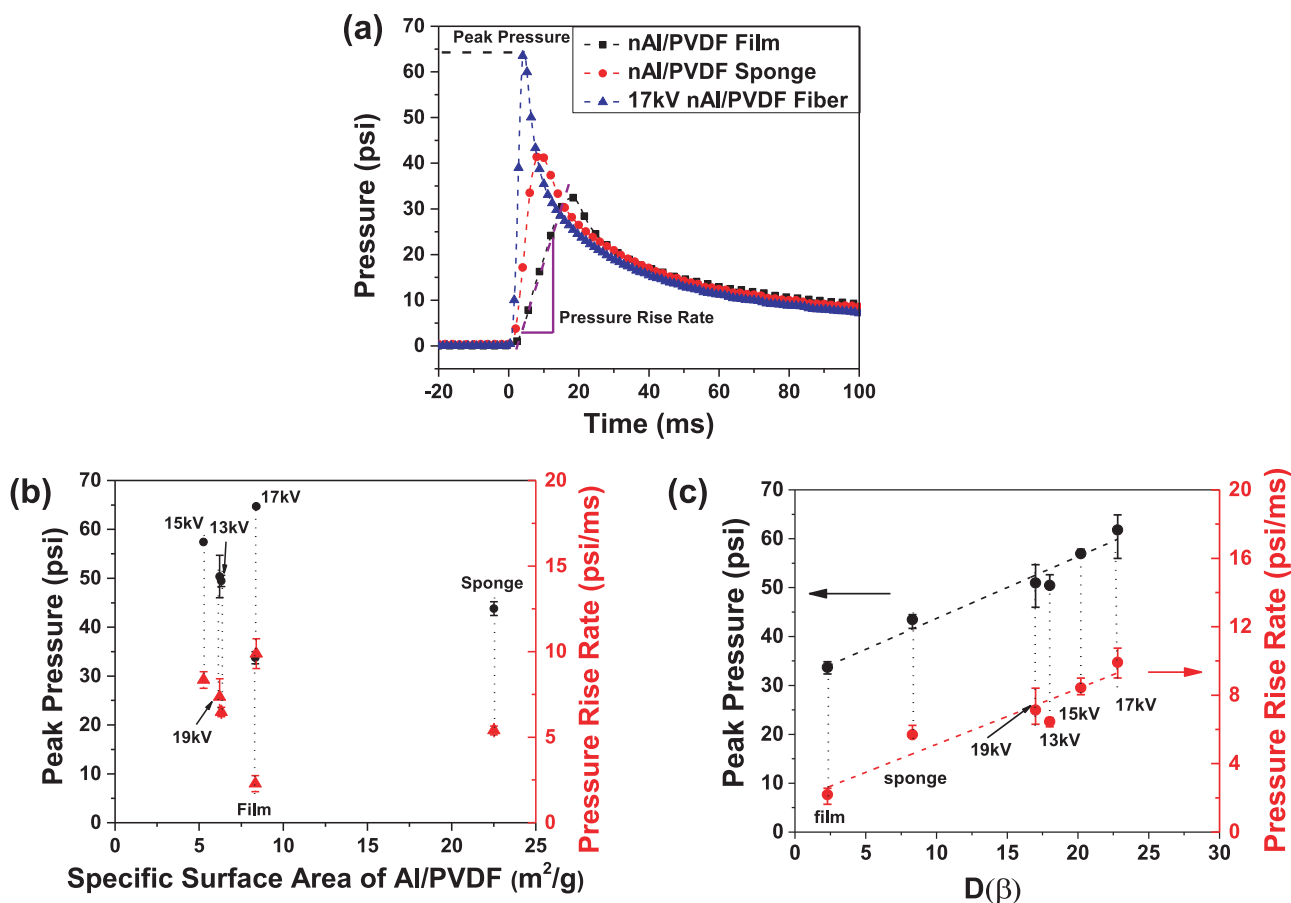
Fig. 4. Comparison of pressure traces of different nAl/PVDF composites ignited in a constant-volume vessel. (a) Representative pressure-time traces of the compressed pellets of nAl/PVDF film, nAl/PVDF sponge and nAl/PVDF fiber (electro-spun at 17kV). Peak pressures and pressure rise rates of compressed nAl/PVDF composites as a function of their (b) specific BET surface area and mass fraction of β-PVDF in PVDF (D(β)). Peak pressures and pressure rise rates show no correlation with specific surface area, but they increase with increasing D(β).
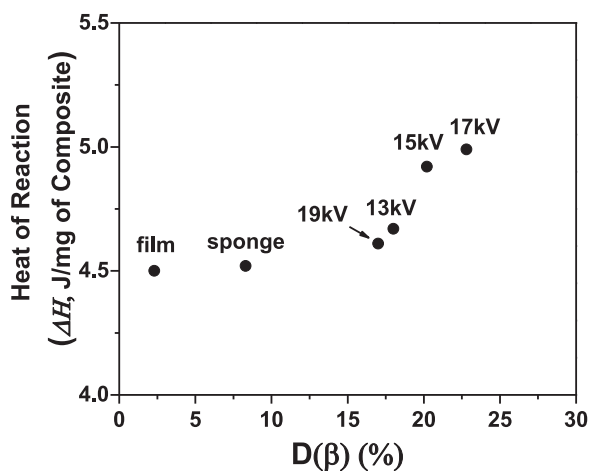
Fig. 5. The heat of reactions of different stochiometric nAl/PVDF composites is plotted against the mass fraction of β-PVDF in PVDF (D(β)).

the Al_2O_3/β-PVDF system, Al-F bonds increase further at temperature ranges between 300 K – 600 K, when compared to the Al_2O_3/α-PVDF system or the Al_2O_3/γ-PVDF system. Also, the number of Al-C (or Al-H) bonds slightly increases, when compared to the Al_2O_3/α-PVDF system or the Al_2O_3/γ-PVDF system (see Fig. 8(a)–(c) for comparison). Meanwhile, the rates of decrease in C-F and C-H bonds in the Al_2O_3/β-PVDF system are faster than the

Al_2O_3/α-PVDF system or the Al_2O_3/γ-PVDF system (see Fig. 8(d)–(f) for comparison).

In addition, we performed the same RMD simulations of the reactivities of α-, β-, and γ-PVDF with an Al slab (see Figs. S5–7 in the Supporting Information), and similar trends to those observed on the Al_2O_3 surface are exhibited. Note that the Al-F bond strength (~ 7.00 eV) is known to be much stronger than the Al-H bond strength (~ 2.99 eV) [51]. Our reactive force field (ReaxFF) qualitatively captures the difference between the Al-F (Fig. S8) and Al-H bond strengths [52]. Given the results and observations above, we confirm that the reactivity of the Al_2O_3 (or Al)/β-PVDF is higher than that of the Al_2O_3 (or Al)/α-PVDF or the Al_2O_3 (or Al)/γ-PVDF, increasing the amount of Al-F and Al-C bonds during the combustion process (e.g., faster reaction rates), hence resulting in higher peak pressure, pressure rise rate, and heat of reaction.

The difference in the reactivity of α-, β-, and γ-PVDF can be explained by their binding energy onto the Al surface. Our ReaxFF calculations show that β-PVDF has stronger binding energy to the Al surface (5.80 eV), compared with Al/α-PVDF (5.10 eV) and Al/γ-PVDF (5.09 eV) systems. These trends are quantitatively consistent with our molecular dynamics calculation in the Supporting Information (Fig. S9). The binding energy difference originates from differences in molecular structure. The β-PVDF has F atoms on one side and H atoms on the other side. Both α-PVDF and γ-PVDF have H and F atoms at both sides. Since the Al-F bond strength (~ 7.00 eV) is known to be much stronger than the Al-H bond strength (~ 2.99 eV) [51], β-PVDF has a stronger binding to the Al surfaces which encourages more Al-PVDF interactions. As such,
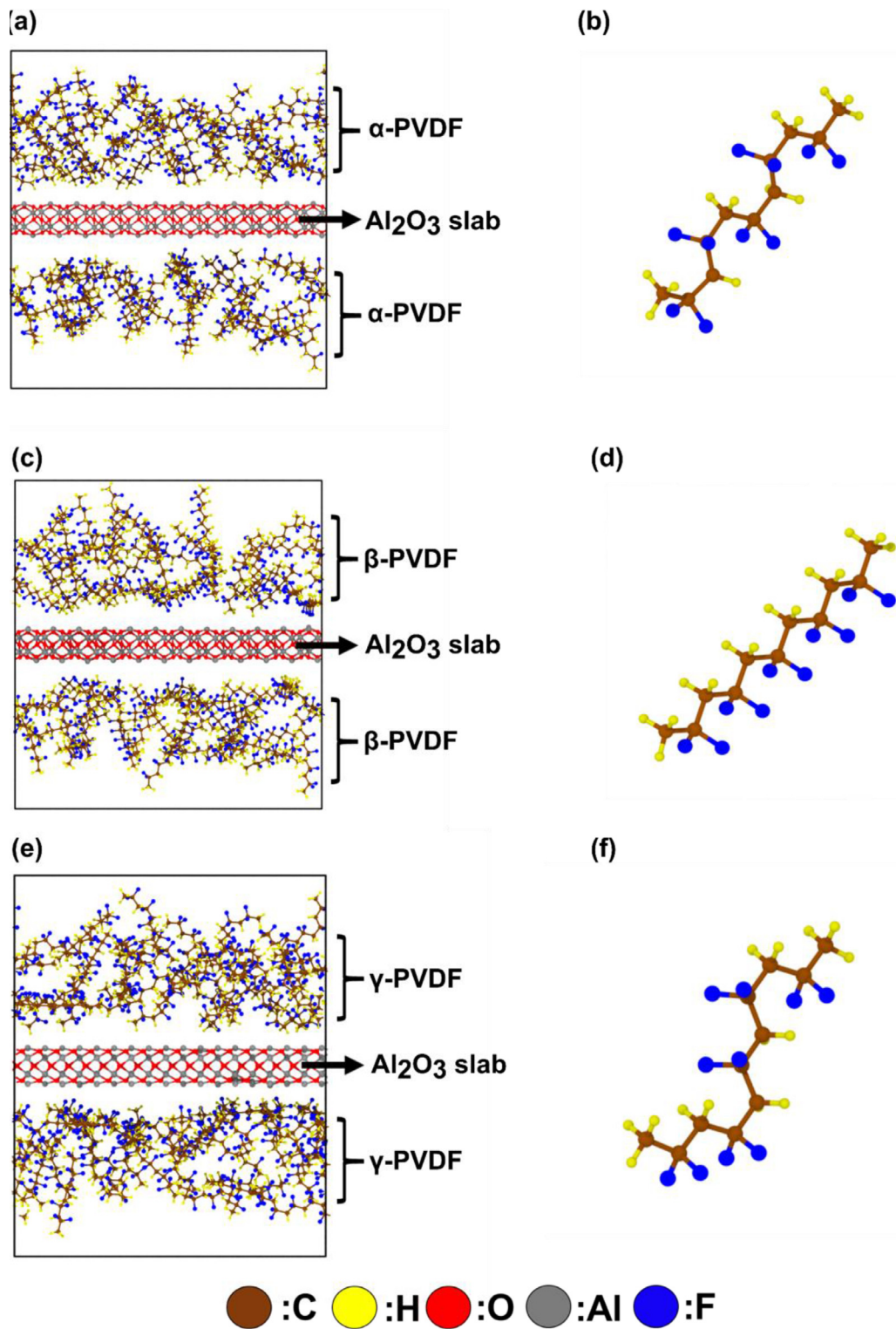
Fig. 6. Computational models for RMD simulations: Al_2O_3 slab in the middle of the simulation domain and crystalline PVDF molecules randomly distributed in the remaining vacuum layers. (a) and (b) configuration for and molecular structure of α-PVDF; (c) and (d) configuration for and molecular structure of β-PVDF; (e) and (f) configuration for and molecular structure of γ-PVDF.
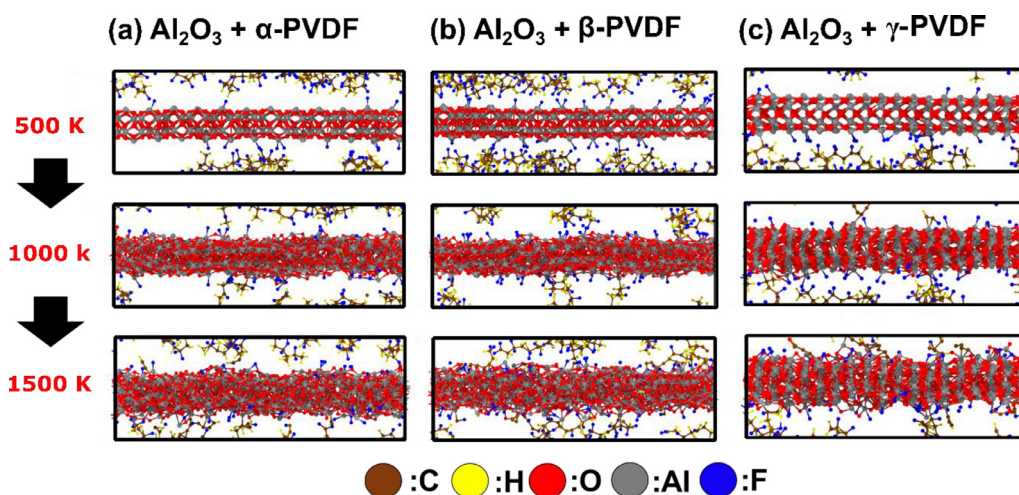
Fig. 7. Snapshots of RMD simulations for reactions of (a) Al_2O_3 slab and α-PVDF molecules; (b) Al_2O_3 slab and β-PVDF molecules; (c) Al_2O_3 slab and γ-PVDF molecules at three temperatures (500K, 1000K, and 1500K). Note that among three different systems, the $Al_2O_3 + \beta$-PVDF system shows the highest reactivity as the increased number of F (blue), C (Brown), or H (Yellows) atoms can be observed in the $Al_2O_3 + \beta$-PVDF system at 1500 K, compared with $Al_2O_3 + \alpha$-PVDF (or Al_2O_3 slab and γ-PVDF) system. The exact amount of each bond population is described in Fig. 8. (For interpretation of the references to color in this figure legend, the reader is referred to the web version of this article.)
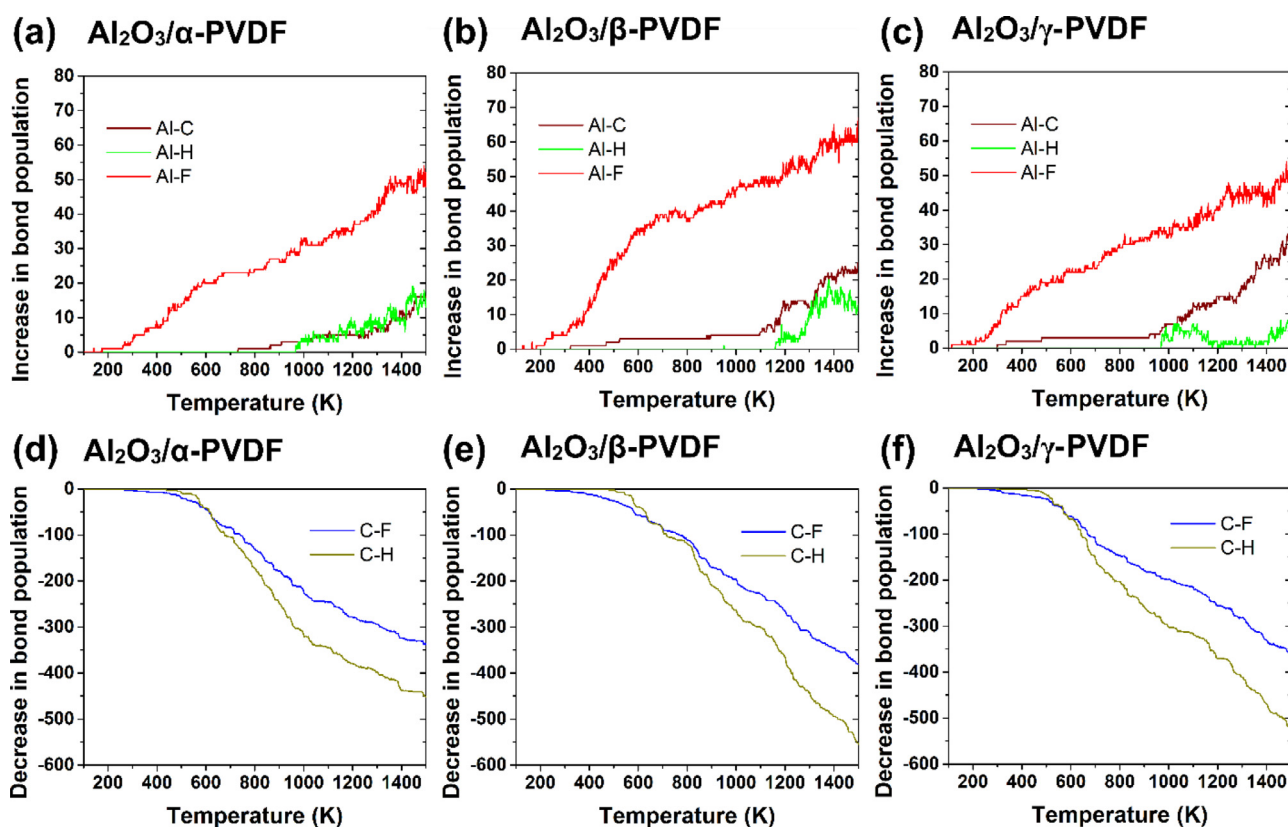

Fig. 8. Increases in Al–C, Al–H, and Al–F bond populations as a function of temperature for (a) Al_2O_3/α-PVDF system, (b) Al_2O_3/β-PVDF system, and (c) Al_2O_3/γ-PVDF system; decreases in C–F and C–H bond populations as a function of time for (d) the Al_2O_3/α-PVDF system, (e) the Al_2O_3/β-PVDF system, and (f) the Al_2O_3/γ-PVDF system.

our computational results can aid in explaining how the combustion performance of nAl/PVDF composites could be improved by β-PVDF modification at the molecular level.

4. Conclusions

We have examined the effect of the crystalline phase of PVDF on the reaction characteristics of nAl/PVDF composites through experiments and RMD simulations. Our experimental results show

that the combustion performance of the stoichiometric nAl/PVDF composites, in terms of peak pressure, pressure rise rate, and heat of reaction, increases with increasing mass fraction of β-PVDF. The combustion performance shows little correlation with the mass fraction of either α- or γ-PVDF. Our RMD simulation results demonstrate that β-PVDF has higher reactivity with both Al_2O_3 and Al than α- and γ-PVDF. The higher reactivity is due to the molecular structure of β-PVDF, which has all the F atoms on one side and has a strong Al-F interaction. Our research points

out a viable method for optimizing the reactive performance of nAl/PVDF composites: increasing the mass content of β-PVDF. This method is expected to be valid for other metal/PVDF composites as well.

Supporting information

Supporting information is available free of charge

SEM images of nAl/PVDF fibers electro-spun at different voltages, XRD spectra of post-combustion products of different nAl/PVDF composites, peak pressures, pressure rise rates, and heat of reactions of nAl/PVDF composites as functions of D(α) and D(γ), RMD simulations of Al-PVDF reactions, and ReaxFF reactive force field development for nAl/PVDF interactions. (PDF)

ReaxFF reactive force field parameters for Al/C/H/O/F interactions (TXT)

Declaration of Competing Interest

The authors declare that they have no known competing financial interests or personal relationships that could have appeared to influence the work reported in this paper.

Acknowledgments

Supplementary materials

Supplementary material associated with this article can be found, in the online version, at doi:10.1016/j.combustflame.2020.06.011.

References

[1] D. Sundaram, V. Yang, R.A. Yetter, Metal-based nanoenergetic materials: synthesis, properties, and applications, Prog. Energy Combust. Sci. 61 (2017) 293–365.

[2] E.L. Dreizin, Metal-based reactive nanomaterials, Prog. Energy Combust. Sci. 35 (2009) 141–167.

[3] R.A. Yetter, G.A. Risha, S.F Son, Metal particle combustion and nanotechnology, Proc. Combust. Inst. 32 (2009) 1819–1838.

[4] W. He, P.-J. Liu, G.-Q. He, M. Gozin, Q.-L. Yan, Highly Reactive metastable intermixed composites (MICs): preparation and characterization, Adv. Mater. 30 (2018) 1706293.

[5] S.M. Umbrajkar, M. Schoenitz, E.L. Dreizin, Exothermic reactions in Al–CuO nanocomposites, Thermochim. Acta 451 (2006) 34–43.

[6] A. Ermoline, M. Schoenitz, E.L. Dreizin, Reactions leading to ignition in fully dense nanocomposite Al-oxide systems, Combust. Flame 158 (2011) 1076–1083.

[7] C. Wu, K. Sullivan, S. Chowdhury, G. Jian, L. Zhou, M.R. Zachariah, Encapsulation of perchlorate salts within metal oxides for application as nanoenergetic oxidizers, Adv. Funct. Mater. 22 (2012) 78–85.

[8] D.T. Osborne, M.L. Pantoya, Effect of Al particle size on the thermal degradation of Al/teflon mixtures, Combust. Sci. Technol. 179 (2007) 1467–1480.

[9] S.K. Valluri, M. Schoenitz, E. Dreizin, Fluorine-containing oxidizers for metal fuels in energetic formulations, Def. Technol. 15 (2019) 1–22.

[10] C. Eldsäter, E. Malmström, Binder materials for green propellants, in: T. Brinck (Ed.), Green Energetic Materials, John Wiley & Sons, Ltd, 2014, pp. 205–234.

[11] C.A. Crouse, Fluorinated polymers as oxidizers for energetic composites, Adv. Fluor. – Contain. Polym. Am. Chem. Soc. (2012) 127–140.

[12] Y. Jiang, S. Deng, S. Hong, S. Tiwari, H. Chen, K. Nomura, R.K. Kalia, A. Nakano, P. Vashishta, M.R. Zachariah, X. Zheng, Synergistically chemical and thermal Coupling between graphene oxide and graphene fluoride for enhancing aluminum combustion, ACS Appl. Mater. Interfaces 12 (2020) 7451–7458.

[13] H. Wang, M. Rehwoldt, D.J. Kline, T. Wu, P. Wang, M.R. Zachariah, Comparison study of the ignition and combustion characteristics of directly-written Al/PVDF, Al/Viton and Al/THV composites, Combust. Flame 201 (2019) 181–186.

[14] S.K. Valluri, M. Schoenitz, E.L. Dreizin, Metal-rich aluminum–polytetrafluoroethylene reactive composite powders prepared by mechanical milling at different temperatures, J. Mater. Sci. 52 (2017) 7452–7465.

[15] X. Ke, S. Guo, G. Zhang, X. Zhou, L. Xiao, G. Hao, N. Wang, W. Jiang, Safe preparation, energetic performance and reaction mechanism of corrosion-resistant Al/PVDF nanocomposite films,, J. Mater. Chem. A 6 (2018) 17713–17723.

[16] C. Huang, G. Jian, J.B. DeLisio, H. Wang, M.R. Zachariah, Electrospray deposition of energetic polymer nanocomposites with high mass particle loadings: a prelude to 3d printing of rocket motors, Adv. Eng. Mater. 17 (2015) 95–101.

[17] J.B. DeLisio, X. Hu, T. Wu, G.C. Egan, G. Young, M.R. Zachariah, Probing the reaction mechanism of aluminum/poly(vinylidene fluoride) composites,, J. Phys. Chem. B 120 (2016) 5534–5542.

[18] J. McCollum, A.M. Morey, S.T. Iacono, Morphological and combustion study of interface effects in aluminum-poly(vinylidene fluoride) composites, Mater. Des. 134 (2017) 64–70.

[19] K.W. Watson, M.L. Pantoya, V.I. Levitas, Fast reactions with nano- and micrometer aluminum: a study on oxidation versus fluorination, Combust. Flame 155 (2008) 619–634.

[20] H. Wang, J.B. DeLisio, S. Holdren, T. Wu, Y. Yang, J. Hu, M.R. Zachariah, Mesoporous silica spheres incorporated aluminum/poly (vinylidene fluoride) for enhanced burning propellants, Adv. Eng. Mater. 20 (2018) 1700547.

[21] S. Huang, M. Pan, S. Deng, Y. Jiang, J. Zhao, B. Levy-Wendt, S.K.Y. Tang, X. Zheng, Modified micro-emulsion synthesis of highly dispersed Al/PVDF composites with enhanced combustion properties, Adv. Eng. Mater. 0 (2019) 1801330.

[22] H. Wang, D.J. Kline, M. Rehwoldt, T. Wu, W. Zhao, X. Wang, M.R. Zachariah, Architecture can significantly alter the energy release rate from nanocomposite energetics, ACS Appl. Polym. Mater. (2019) accessed April 11, 2019.

[23] A.J. Lovinger, Ferroelectric Polymers, Science. 220 (1983) 1115–1121.

[24] P. Martins, A.C. Lopes, S. Lanceros-Mendez, Electroactive phases of poly(vinylidene fluoride): determination, processing and applications, Prog. Polym. Sci. 39 (2014) 683–706.

[25] X. Cai, T. Lei, D. Sun, L. Lin, A critical analysis of the α, β and γ phases in poly(vinylidene fluoride) using FTIR, RSC Adv. 7 (2017) 15382–15389.

[26] J. Zheng, A. He, J. Li, C.C. Han, Polymorphism control of poly(vinylidene fluoride) through electrospinning, Macromol. Rapid Commun. 28 (2007) 2159–2162.

[27] J.N. Maycock, D.E. Grabenstein, Piezoelectricity in secondary explosives, Science 152 (1966) 508–509.

[28] R.S. Janesheski, L.J. Groven, S Son, Fluoropolymer and aluminum piezoelectric reactives, AIP Conf. Proc. 1426 (2012) 741–744.

[29] S.L. Row, L.J. Groven, Smart energetics: sensitization of the aluminum-fluoropolymer reactive system, Adv. Eng. Mater. 20 (2018) 1700409.

[30] H. Su, A. Strachan, W.A. Goddard, Density functional theory and molecular dynamics studies of electroactive polymers: PVDF and P(VDF-TrFE), Phys. Rev. B. 70 (2004) 064101.

[31] R. Hasegawa, M. Kobayashi, H. Tadokoro, Molecular conformation and packing of poly(vinylidene fluoride). stability of three crystalline forms and the effect of high pressure, Polymer J. 3 (1972) 591.

[32] S. Huang, S. Deng, Y. Jiang, X. Zheng, Experimental effective metal oxides to enhance boron combustion, Combust. Flame 205 (2019) 278–285.

[33] Y. Jiang, S. Deng, S. Hong, J. Zhao, S. Huang, C.-C. Wu, J.L. Gottfried, K. Nomura, Y. Li, S. Tiwari, R.K. Kalia, P. Vashishta, A. Nakano, X. Zheng, Energetic performance of optically activated aluminum/graphene oxide composites, ACS Nano 12 (2018) 11366–11375.

[34] V.S. Parimi, S. Huang, X. Zheng, Enhancing ignition and combustion of micron-sized aluminum by adding porous silicon, Proc. Combust. Inst. 36 (2017) 2317–2324.

[35] A.C.T. van Duin, S. Dasgupta, F. Lorant, W.A. Goddard, ReaxFF: a reactive force field for hydrocarbons,, J. Phys. Chem. A 105 (2001) 9396–9409.

[36] T.P. Senftle, S. Hong, M.M. Islam, S.B. Kylasa, Y. Zheng, Y.K. Shin, C. Junkermeier, R. Engel-Herbert, M.J. Janik, H.M. Aktulga, T. Verstraelen, A. Grama, A.C.T. van Duin, The ReaxFF reactive force-field: development, applications and future directions, Npj Comput. Mater. 2 (2016) 15011.

[37] S. Hong, A.C.T. van Duin, Atomistic-scale analysis of carbon coating and its effect on the oxidation of aluminum nanoparticles by reaxff-molecular dynamics simulations, J. Phys. Chem. C 120 (2016) 9464–9474.

[38] A. Rahnamoun, A.C.T. van Duin, Reactive molecular dynamics simulation on the disintegration of Kapton, POSS polyimide, amorphous silica, and teflon during atomic oxygen impact using the reaxff reactive force-field method,, J. Phys. Chem. A 118 (2014) 2780–2787.

[39] S.-Y. Kim, A.C.T. van Duin, J.D. Kubicki, Molecular dynamics simulations of the interactions between TiO2 nanoparticles and water with Na+ and Cl−, methanol, and formic acid using a reactive force field, J. Mater. Res. 28 (2013) 513–520.

[40] S. Nosé, A unified formulation of the constant temperature molecular dynamics methods,, J. Chem. Phys. 81 (1984) 511–519.

[41] W.G. Hoover, Canonical dynamics: Equilibrium phase-space distributions, Phys. Rev. A 31 (1985) 1695–1697.

[42] E. Kabir, M. Khatun, L. Nasrin, M.J. Raihan, M. Rahman, Pure beta phase formation in polyvinylidene fluoride (PVDF)-carbon nanotube composites,, J. Phys. D: Appl. Phys. 50 (2017) 163002.

[43] L.F. Malmonge, L.H.C. Mattoso, Thermal analysis of conductive blends of PVDF and poly(o-methoxyaniline), Polymer 41 (2000) 8387–8391.

[44] J. Liu, X. Lu, C. Wu, Effect of preparation methods on crystallization behavior and tensile strength of poly(vinylidene fluoride) membranes, Membranes 3 (2013) 389–405.

[45] W. Zhou, J. Zuo, W. Ren, Thermal conductivity and dielectric properties of Al/PVDF composites, Compos. A: Appl. Sci. Manuf. 43 (2012) 658–664.

[46] V. Sencadas, R.G. Jr, S. Lanceros-Méndez, α to β phase transformation and microstructural changes of PVDF films induced by uniaxial stretch, J. Macromol. Sci. B 48 (2009) 514–525.

[47] V.F. Cardoso, G. Minas, C.M. Costa, C.J. Tavares, S. Lanceros-Mendez, Micro and nanofilms of poly(vinylidene fluoride) with controlled thickness, morphology and electroactive crystalline phase for sensor and actuator applications, Smart Mater. Struct. 20 (2011) 087002.

[48] L. Glavier, G. Taton, J.-M. Ducéré, V. Baijot, S. Pinon, T. Calais, A. Estève, M. Djafari Rouhani, C. Rossi, Nanoenergetics as pressure generator for nontoxic impact primers: Comparison of Al/Bi2O3, Al/CuO, Al/MoO3 nanothermites and Al/PTFE, Combust. Flame 162 (2015) 1813–1820.

[49] S. Hong, A.C.T. van Duin, Molecular dynamics simulations of the oxidation of aluminum nanoparticles using the ReaxFF reactive force field„ J. Phys. Chem. C 119 (2015) 17876–17886.

[50] L.P.H. Jeurgens, W.G. Sloof, F.D. Tichelaar, E.J. Mittemeijer, Growth kinetics and mechanisms of aluminum-oxide films formed by thermal oxidation of aluminum, J. Appl. Phys. 92 (2002) 1649–1656.

[51] Y.-R. Luo, Comprehensive Handbook of Chemical Bond Energies, CRC Press, 2007.

[52] J.G.O. Ojwang, R.A. van Santen, G.J. Kramer, A.C.T. van Duin, W.A. Goddard, Parametrization of a reactive force field for aluminum hydride„ J. Chem. Phys. 131 (2009) 044501.